# Silicon based On-chip Sub-Wavelength Grating Ring and Racetrack Resonator BioSensors

Hai Yan,[1,†] Lijun Huang,[2,†] Xiaochuan Xu,[3,*,†] Naimei Tang,[3] Swapnajit Chakravarty,[3] Huiping Tian,[2] and Ray T. Chen[1,3,*]

[1]Department of Electrical and Computer Engineering, The University of Texas at Austin, Austin, TX 78758, USA
[2]State Key Laboratory of Information Photonics and Optical Communications, School of Information and Communication Engineering, Beijing University of Posts and Telecommunications, Beijing 100876, China
[3]Omega Optics Inc., 8500 Shoal Creek Blvd., Bldg. 4, Suite 200, Austin, TX, 78757, USA
*Corresponding author: xiaochuan.xu@omegaoptics.com;raychen@uts.cc.utexas.edu
[†]These authors contributed equally to this paper.

## ABSTRACT

In this paper, we experimentally study the unique surface sensing property and enhanced sensitivity in subwavelength grating (SWG) based microring resonator biosensors versus conventional ring resonator biosensors. In contrast to a conventional ring, the effective sensing region in the SWG microring resonator includes not only the top and side of the waveguide, but also the space between the silicon pillars on the propagation path of the optical mode. It leads to an unique property of thickness-independent surface sensitivity versus common evanescent wave sensors; in other words, the surface sensitivity remains constantly high with progressive attachment of biomolecules to the sensor surface. To increase the robustness of performance of ring shaped circular SWG biosensors, we experimentally demonstrate silicon SWG racetrack resonators. A quality factor of 9800 and bulk sensitivity (S) is ~429.7 nm/RIU (refractive index per unit) results in an intrinsic detection limit (iDL) $3.71 \times 10^{-4}$ RIU in racetrack SWG biosensors while still retaining the accumulated surface thickness properties of circular rings.

## 1. INTRODUCTION

Micro- and nano-scale photonic biosensors have become a fast growing research topic driven by the need of portable bio-detection systems with high sensitivity, high throughput, and real-time and label-free detection [1–3]. Various devices, including surface plasmon devices [4,5], microring resonators [6–8], silicon nanowires [9], nanoporous silicon waveguides [10], one-dimensional (1D) and two-dimensional (2D) photonic crystal (PC) microcavities [11–13], have been proposed and demonstrated. Most proposed structures are based on the interaction between the evanescent wave and the biomolecules that are adsorbed or immobilized on the sensor surface. In the silicon-on-insulator (SOI) platform, significant efforts have been made on various evanescent wave sensors focusing on increasing the sensitivity and lowering the detection limit [14–18]. However, in evanescent wave sensing, the sensitivity drops inevitably with increasing thickness of the surface layer accumulated on the sensor surface with reduced overlap of the optical mode with the analyte. In real applications, this layer includes necessary oxide and chemical layers generated by surface treatment, probe biomarkers, target biomarkers and any other reagents that enhance the signal. The total layer thickness can vary from several nanometers to a few tens of nanometers during experiments.

Recently, novel subwavelength grating (SWG) based waveguides and photonic devices were proposed and demonstrated [19–22]. The SWG waveguide consists of periodic silicon pillars in the propagation direction with a period much smaller than the operating wavelength. In such a structure, the wave propagates similar to conventional strip waveguides, but the interaction region between light and cladding materials is greatly extended. In Ref. [23,24], microring resonators based on SWG waveguides were first demonstrated with bulk sensitivity greater than 400 nm/RIU, which is higher than conventional microring resonators based on strip waveguides. As with other sensors, challenges to further improve the sensitivity of the SWG ring resonator involve the need to optimize the quality factor and the detection limit so that the coupling strength between the bus waveguide and the circular ring resonator can compensate the loss.

In this paper, we describe our recent work with silicon based compact SWG ring and racetrack resonators, while at the same time show their unique surface sensing capability. We show that in SWG resonators, the surface sensitivity remains constantly high when surface layer thickness grows, a significant advantage for biosensors and other surface based sensors.

## 2. SUB-WAVELENGTH GRATING RING RESONATORS

### 2.1. DEVICE SIMULATION

The structure of the SWG microring resonator is shown in Fig. 1(a). The silicon SWG microring resonator is on top of the buried oxide layer and is covered by sensing medium (water or other biological buffers, assuming refractive index $n = 1.32$). Fig. 1(b) shows the top view of the ring-waveguide coupling region. The SWG in the microring resonator uses trapezoidal pillars to minimize bending loss, and achieve better quality factors [25]. The SWG in the bus waveguide still uses regular rectangular pillars [23].
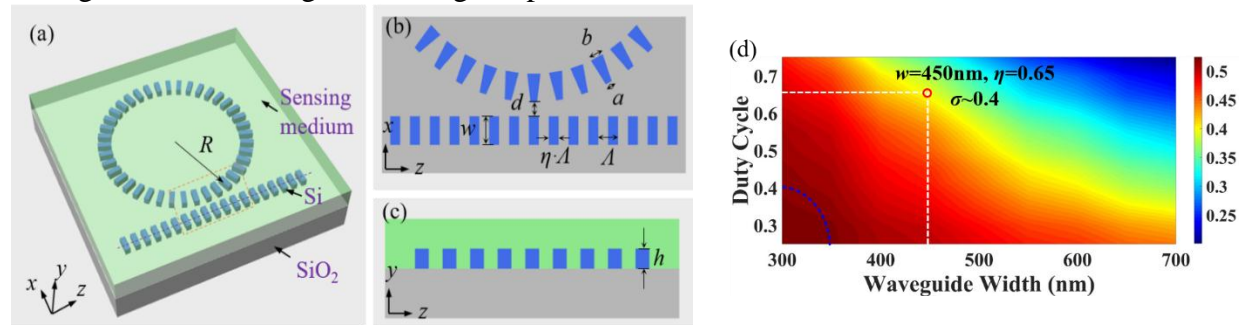


**Figure 1.** (a) Schematic of SWG microring resonator biosensor; (b) Top view of the coupling region (yellow rectangular in (a)); (c) Cross section view of the SWG waveguides (purple cut line in (a)). (d) Overlapping factors for different waveguide width and duty cycle combinations.

The radius of the microring $R$ is set to 10μm to achieve high intrinsic quality factor and compact size at the same time. Grating period of the SWG is $\Lambda = 200$ nm fulfills the condition $\lambda / \Lambda > 2n_{eff}$ ($\lambda = 1550$ nm), so that the waveguide operates in the subwavelength regime and behaves like a conventional waveguide [20]. Duty cycle of the grating (ratio of silicon pillar width to grating period) $\eta$ and waveguide width $w$ are optimized through simulation to maximize the optical field overlap with the sensing medium. The gap between microring and the bus waveguide is $d = 50$nm. For trapezoidal pillars in the SWG microring, grating period and duty cycle are same as the straight waveguide. Widths of the top base (a) and bottom base (b) are

determined by minimizing bending loss in the microring using 3D finite difference time domain (FDTD) simulation [26]. The height of the silicon layer (see Fig. 1(c)) is $h = 220$ nm.

To optimize duty cycle $\eta$ and waveguide width $w$, the optical mode profile is simulated using the 3D plane wave expansion (PWE) method and the overlapping factor $\sigma$ (defined as the ratio of the electric field inside the low refractive index medium region) is calculated. The results are plotted in Fig. 1(d), in which waveguide width and duty cycle are scanned in $x$ and $y$ axis respectively. The region inside the blue dashed curve indicates modes that are above the silicon dioxide light line and not well-confined. The absorption loss of light in water also contributes to the total loss in the SWG microring and deteriorates its quality factor. Taking both loss and the overlapping factor $\sigma$ into account, $\eta = 0.65$ and $w = 450$ nm resulted in a calculated overlapping factor $\sigma = 0.4$. So the width of the rectangular pillar is $\eta\varLambda = 130$ nm. The optimized $a=100$nm and $b=150$nm are determined through bending loss simulation as described above.
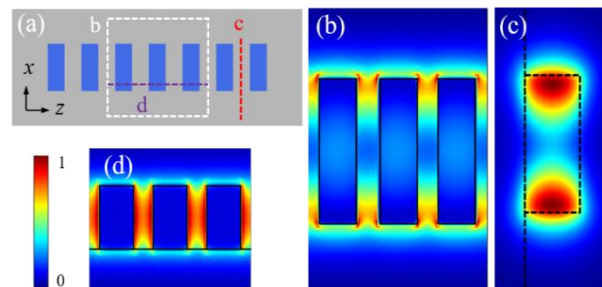


**Figure 2.** Transverse electric (TE) polarized electric field intensity distribution at different cross sections. (b)- (d) correspond to the cut positions marked with b, c, d in the schematic (a).

The TE mode profile simulated with the above parameters is shown in Fig. 2. Fig. 2(a) illustrates the schematic of the SWG structure. TE mode profiles at cut planes b-d are shown in Fig. 2(b-d), respectively. Fig. 2(b) is the electric field distribution at the middle height of the pillar ($xy$ plane at $y=h/2$); Fig. 2(c) shows the electric field between pillars ($xy$ plane at $z$=constant); Fig. 2(d) shows the field between pillars cutting close to the edge of the pillar ($yz$ plane at $x$ close to edge of the pillar). From the mode profile, it can be seen that in addition to the top surface and sidewalls of the waveguide, where evanescent wave exists, a significant portion of the mode field exists on the light propagation path between silicon pillars. This gives SWG waveguide based microring biosensors extended sensing region and thus unique advantage for surface sensing over conventional microrings.

In a ring resonator biosensor, resonance wavelength shifts as biomolecules immobilize on the surface of the microring resonators through biochemical interactions. Fig. 3(a) shows a schematic for a sensor on the SWG structure. The surface layer thickness ranges from few nanometers to several tens of nanometers [23,27–30], including surface oxide layer (~5nm), chemical layer (several nanometers, generated after surface treatment with (3-Aminopropyl) triethoxysilane (APTES), glutaraldehyde, etc.) and protein layers (antibodies, antigens, etc., several nanometers per layer). Therefore, surface sensitivity is an important figure of merit.

In resonance based sensing method, surface sensitivity $S_s$ can be defined as the resonance wavelength shift in according to the surface layer thickness change [24]:

$$S_s = \frac{\Delta\lambda}{\Delta t} = \frac{\lambda}{n_g}\left(\frac{\partial n_{eff}}{\partial t}\right) \qquad (1)$$

where $n_g$ is group index, $t$ is the thickness of surface layer. As shown in Fig.3(a), we assume the sensing medium is water ($n = 1.32$) and the surface layer has uniform thickness in all direction with uniform refractive index of $n=1.48$ [20,23,31]. The susceptibility $\partial n_{eff} / \partial t$ in periodic SWG structure is calculated from effective index ($n_{eff}$) simulation results using the 3D PWE solver.
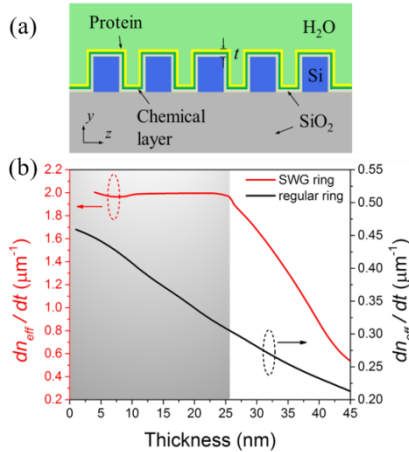


**Figure 3.** (a) Schematic of the SWG structure covered by a thin layer of immobilized protein in water environment; (b) Comparing $dn_{eff}/dt$ as the surface layer thickness grows.

The SWG structure has the same parameters presented above. $\partial n_{eff} / \partial t$ in conventional strip waveguide ($w = 500$ nm, $h = 220$ nm) (used to form regular microring resonator) is calculated in an eigenmode solver using finite element method (FEM). The results are shown in Fig. 3(b). The $\partial n_{eff} / \partial t$ in SWG waveguide is 4-6 times larger than that in a regular strip waveguide due to large mode overlapping factor ($\sigma \sim 0.4$). Furthermore, the value remains constantly high in SWG structure for the first 25nm of the surface layer, while in regular strip waveguide, $\partial n_{eff} / \partial t$ drop monotonically with the accumulation of surface layer. This simulation results coincide with the above mode profile simulation and analysis that SWG structure has superior surface sensing capabilities over evanescent wave based sensors like conventional microring resonator, in terms of both absolute surface sensitivity $S_s$ and the ability to maintain high surface sensitivity when surface layer thickness grows.

## 2.2 SENSING EXPERIMENT METHODS

Device fabrication has been described extensively in past work. [23, 24] To characterize the bulk refractive index sensitivity of the proposed SWG microring resonator, different concentrations of glycerol in water solution (0%, 5%, 10%, 20%, v/v) were prepared and flowed onto the chip through microfluidic channels. The resonance wavelengths were recorded and the sensitivity was calculated by $S = \Delta\lambda / \Delta n$, the resonance shift versus refractive index change. Refractive index data was obtained from Ref. [32].

Both SWG microring resonator and conventional microring resonator were fabricated on the same chip and characterized. The chip was first silanized by 2% (v/v) (3-Aminopropyl) triethoxysilane (APTES) in toluene. Then the chip was further treated with 2.5% (v/v) glutaraldehyde in phosphate buffer saline (PBS) to provide aldehyde group linker that is able to immobilize protein covalently [28,30]. Next, anti-streptavidin antibody (50ug/mL, from Abcam), bovine serum albumin (BSA, 1mg/mL), streptavidin (100ug/mL, from Sigma-Aldrich), and

biotinylated BSA (1mg/mL, from Thermo Fisher Scientific) were flowed to both microring sensors in order. Anti-streptavidin antibody was immobilized on the sensor surface as probe protein. BSA was used as blocking buffer to block any vacant sites. Streptavidin binds to probe protein and later capture biotinylated BSA through biochemical interactions. Before switching reagent at each of the above steps, PBS buffer was flowed to remove any unbound biomolecules. Resonance wavelengths of both the SWG and conventional microring resonator were recorded and resonance shifts were compared.

## 2.3. Results and Discussion

Scanning electron microscope images of the fabricated SWG microring resonator are shown in Fig. 4(a). Transmission spectrum of the SWG microring is shown in Fig. 4(b), from which the free spectral range is measured to be 12.5nm, corresponding to group index $n_g = \lambda^2 / (2\pi R \cdot FSR) = 3.0$. The estimated quality factor ($Q \sim \lambda / \delta\lambda$) is as high as 9100 due to the use of trapezoidal pillars in the SWG microring which reduces bending loss [25]. Next, bulk refractive index sensitivity of the SWG microring biosensor was characterized. The resonance peak wavelength was monitored during the experiment and plotted in Fig. 4(c). Thus, the bulk sensitivity can be estimated by a linear fit on the resonance shift versus refractive index change plot, as shown in Fig. 4(d). The fitting shows a bulk sensitivity of $S_b$ = 440.5±4.2 nm/RIU, which is a typical value for SWG microring resonators (slightly lower than that in Ref. 23 due to a larger duty cycle) [23], and about 4 times of that of a regular microring resonator [6]. Considering the high quality factor, the intrinsic detection limit of the sensor $DL = \lambda / (Q \cdot S_b)$ is $3.9 \times 10^{-4}$ RIU. To demonstrate the enhanced surface sensitivity in SWG microring resonators, both SWG microring resonator and regular microring resonator were fabricated on the same chip and compared in a surface sensing test. The regular microring resonator has the same radius of 10 μm and the waveguide is 450 nm wide and 220 nm high.

Fig. 5(a) presents the real time monitoring of the resonance shift in SWG microring biosensor. Regions with blue background indicate PBS buffer washing steps between the flow of different reagents. The steps of flowing different reagents are marked with corresponding names in the figure. The gradual red-shift of resonance during reagents flow steps reflects the continuous binding of biomolecules to the chemically treated surface or to its conjugated biomolecules. PBS buffer removes unattached biomolecules and create the same background refractive index so that the resonances can be compared at each step. The resonance shifts of regular microring were also recorded at each buffer washing step. The slightly different curve in the biotinylated BSA step was probably caused by an nonuniform concentration in the solution, but did not affect the following results. The resonance shifts for both microring biosensors are shown in Fig. 5(b). Resonance shift in SWG microring are several times larger than that in regular microring as expected, because of the much larger optical overlap integrals in SWG microring. It is also seen that with increasing layers on the surface, the Δλ difference between the two microrings also becomes larger.

To explicitly show this difference, surface sensitivity with respect to surface layer thickness is compared in both rings as shown in Fig. 5(c). The thickness of the surface layers is estimated by combining the simulated surface sensitivity and the experimental resonance shift in SWG microring. According to Equation (1) and the simulation in Fig. 3(b), the surface sensitivity of the SWG ring is $S_s \approx 1.0 nm/nm$ ($\lambda$ = 1550 nm, $n_g$ = 3.0, assume $n$ = 1.48 across all surface

layer [20,23,31]) for the first 25 nm thick of surface layer. Therefore the surface layer thickness can be estimated. The surface sensitivity of the regular microring can then be calculated by the first part of Equation (1). Fig. 5(c) shows that the sensitivity of the microring resonator drops monotonically compared to that of the SWG ring as thickness of accumulated biomolecules grows continuously. Since both devices were tested side by side in the same microfluidic channel, the surface layer thickness can be assumed as the same; thus the resonance shift at each thickness can be compared. The thickness in Fig. 5(c) also takes into account the initial thickness of silicon dioxide (~5nm) and APTES (~5nm).
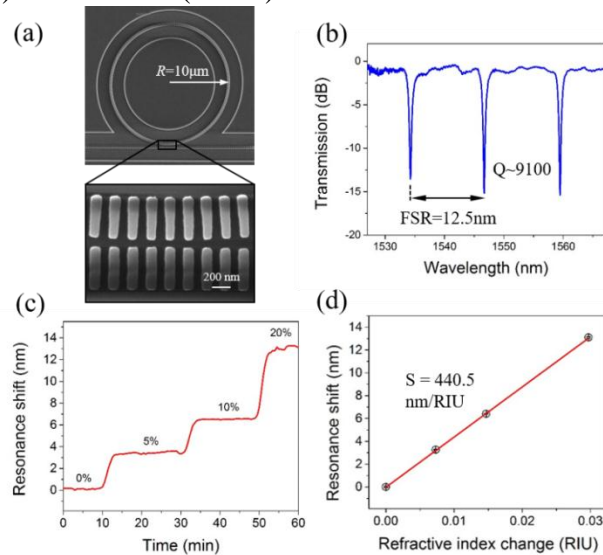


**Figure 4.** (a) Scanning electron microscope image of the SWG microring resonator with its coupling region enlarged. (b) transmission spectrum of the fabricated SWG microring resonator; (c) Resonance wavelength shift during the bulk refractive index sensing test; (d) Resonance shift with respect to refractive index change. Linear fit shows a bulk sensitivity ~ 440.5 nm/RIU.
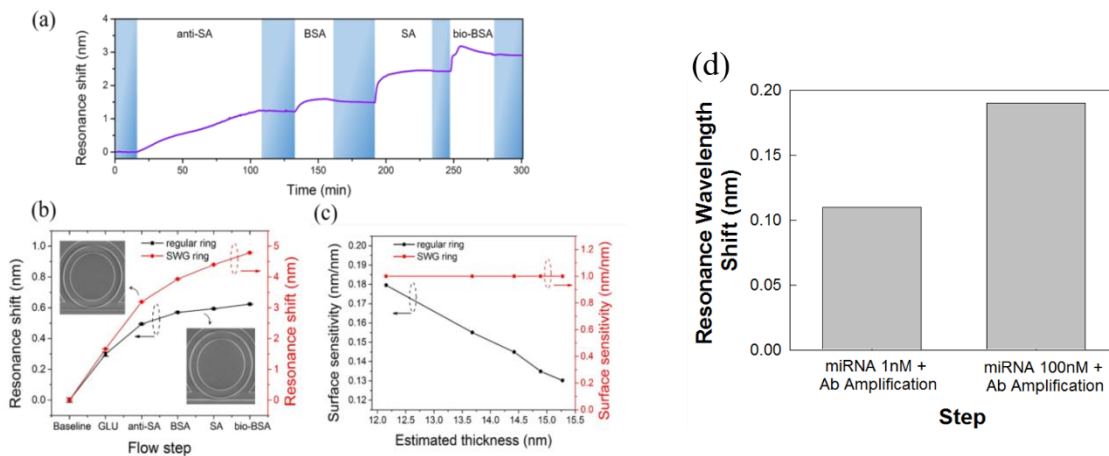


**Figure 5.** (a) Real time monitoring of resonance shift in SWG microring biosensor; Blue region indicate buffer washing steps and other steps are marked with corresponding reagents used. Anti-SA: anti-streptavidin antibody, SA: streptavidin, bio-BSA: biotinylated BSA. (b) Resonance shift in SWG microring and regular microring; insets show SEM images of microrings; GLU: glutaraldehyde (c) Surface sensitivity with respect to estimated thickness in both SWG microring and regular microring. (d) Resonance wavelength shift in miRNA sensing experiment.

The SWG microring resonator was also used to detect low concentrations of microRNA (miRNA). The chip containing SWG microring biosensors was chemically modified with APTES and glutaraldehyde as described above. Then capture DNA (1mM) was flowed on the sensor surface followed by blocking buffer. The conjugate miRNA (1nM and 100nM) was then flowed in the microfluidic channels followed by anti-DNA:RNA antibody to amplify the signal. The test result is shown in Fig. 5(d). A net resonance wavelength shift of 0.11 nm is observed for 1nM miRNA with anti-DNA:RNA antibody amplification. A net resonance wavelength shift of 0.19 nm is observed for 100nM miRNA with antibody amplification. This shows that the SWG microring biosensor is promising in detecting low concentration of biomolecules in real applications.

## 3. SUB-WAVELENGTH GRATING RACETRACK RESONATOR

### 3.1. DEVICE SIMULATION

The 3D schematic of the proposed SWG racetrack resonator is shown in Fig. 6(a). The magnified image between SWG waveguide and SWG racetrack waveguide is shown in Fig. 6(b). The composite SWG core is formed by periodically interleaving high (silicon) and low (analyte solutions) refractive index materials. To get lower eigen-frequency and increase the photo-analyte overlap, a smaller period of 200nm is chosen. In Fig. 6(b), $\Lambda$ represents the period of the SWG structure and equals 200 nm. $L$, $W$ and $H$ are the length, width and thickness of silicon (Si) pillars, respectively. $L_c$ and $G$ represent the coupling length and the gap between the SWG waveguide and racetrack waveguide, respectively. The radius of racetrack is 10μm. The thickness of the buried oxide is 3μm. The upper cladding is the analyte solutions to be detected.
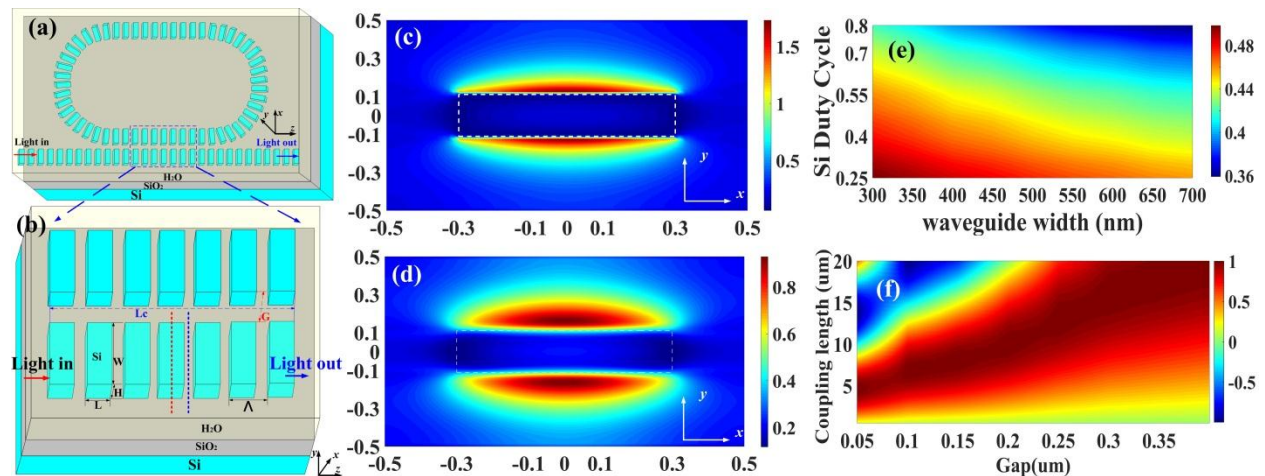


**Figure 6.** (a) 3D schematic of SWG racetrack resonator. (b) The magnified image of the SWG bus waveguide and the SWG racetrack waveguide in rectangular region with a blue dash line. $E_y$ electric fields of TM mode within silicon pillar to enhance light-matter interaction in -x and -y plane in red (c) and blue (d) dash line position in (b) around 1550 nm. (e) Plot of overlap of light and silicon versus duty cycle and width of Si pillars. (f) Plot of coupling efficient changing with coupling length $L_c$ and gap $G$ around 1550 nm.

To analyze the electric field outside Si pillars around 1550 nm, TM mode profiles (RSoft 3D BandSOLVE simulations) on *xy* plane at different positions (red and blue dash line in Fig. 6(b)) are shown in Figs. 6(c) and 6(d)). The dimension of the silicon pillar (L×W×H) in this simulation is 140 nm×600nm ×220nm. As seen in Figs. 6(c) and 6(d), the *y* component of the electric field extends into the upper cladding and lower substrate. That means the evanescent field penetrates deeply in the cladding and substrate. The presence of electrical field in analytes is expected to drastically increase the photon-analyte interaction and subsequently enhance both the bulk and surface sensitivity compared with transverse electric (TE) guide modes. However, the increased interaction inevitably causes additional absorption loss by analytes and scattering loss induced by surface roughness. Therefore, a tradeoff between the photon-analyte interaction and optical loss need to be considered in optimizing the design.

In order to quantify the photon-analyte interaction, we calculate the overlap integral *f* between the optical field and the analytes while varying the size of pillars. The overlap integral is defined as: [33]

$$ f = \frac{\int_{V_{low\ index}} \varepsilon \left| \vec{E} \right| dr^3}{\int_{V_{low\ index+dielectric}} \varepsilon \left| \vec{E} \right| dr^3} \qquad (2) $$

Here, the volume integral in the numerator is the electric field energy outside of the Si pillars. The plot of the *f* in relation to the duty cycle and width of pillars is shown in Fig. 6 (e). The *f* increases with decrease of Si duty cycle and the width of pillars, meaning the light confinement in the core is decreased and thus the sensitivity is enhanced. However, the optical loss will increase significantly. The photonic modes approach the light line of the cladding materials and are subject to more radiation loss resulting in quasi-guided modes [34]. We choose a pillar size L×W×H = 140 nm×600nm ×220nm considering the tradeoff between sensitivity and optical loss. The overlap 39.7% of TM modes is larger than 30.2% of TE modes with the same size pillar. Thus, a higher sensitivity for TM mode SWG racetrack resonators is anticipated compared to the TE mode SWG racetrack resonators with the same geometry. We analyze the coupling coefficients between the coupling length ($L_C$) and the gap ($G$) of the racetrack waveguide and subwavelength bus waveguide in RSoft BeamPROP to minimize the influence of light in the racetrack [35]. As shown in Fig. 6(f), larger coupling length is needed when the gap increases to achieve a maximum coupling strength from bus SWG waveguide to the racetrack waveguide, because the coupling strength is weakened as the gap is increased. The critical coupling can be satisfied when gap is 140nm and the coupling length is approximately equal to 6μm by simulations [36, 37]. Specially, the racetrack resonator is a ring resonator when the $L_C$ equals 0. However, the footprint of racetrack resonator is less than that of circular ring with the same circumference.

For TM mode grating couplers, the grating period and Si duty cycle are 850 nm and 0.7 respectively. The SWG period and width of trench are 300 nm and 150 nm respectively. Fig. 7(a) is the optical microscope image of the fabricated SWG racetrack resonator, in which light is coupled into the strip waveguide by the TM grating coupler, then coupled into SWG waveguide by the taper, and coupled out by the other taper and grating coupler. Fig. 7(b) is the scanning electron microscopy (SEM) image of the fabricated SWG racetrack resonator labeled in green dash rectangular in Fig. 7(a). Figs. 7(c), 7(d) and 7(e) are the TM mode grating coupler, the magnified SEM images of the left taper between strip waveguide and SWG waveguide, and the coupling region of the SWG bus waveguide and SWG racetrack waveguide, respectively.

### 3.2. Device Measurements

The fabricated racetrack resonator is measured in DI water and transmission spectrum is shown in Fig. 8 (a). As seen in Fig. 8 (a), the quality factor and the extinction ratio of the fabricated devices are maximized near 1560 nm when the coupling length and gap are 6.5μm and 140 nm respectively. The full-width at half-maximum (FWHM) of the resonance at 1562.9 nm in DI water is 0.16 nm, corresponding to a quality factor of ~9800, and the extinction ratio is about 24.6dB. The optimized coupling length is 6.5μm in fabrication which is slightly different from the simulation results (6 μm). The fabrication induced roughness is possibly the reason for the discrepancy between the simulation and the fabrication.
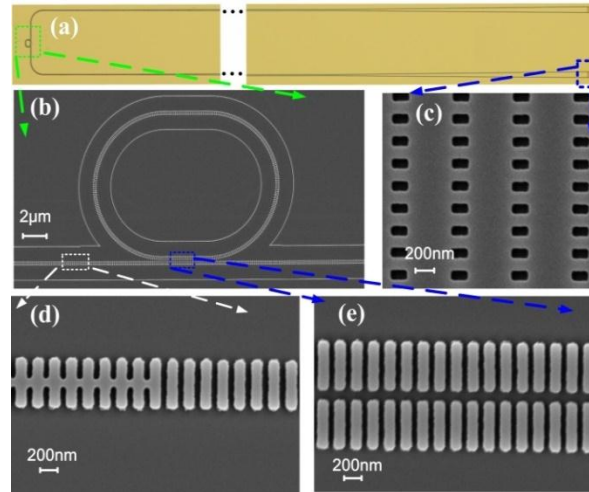


**Figure 7.** (a) Optical microscope image of the fabricated SWG racetrack resonator. (b) Scanning electron images (SEM) of fabricated devicein green dash rectangular region in (a). (c) The TM mode grating coupler in (a). The magnified SEM images of (d) the left taper between strip waveguide and SWG waveguide in white dash rectangular region, and (e) the coupling region between the SWG bus waveguide and racetrack waveguide in blue dash rectangular region.
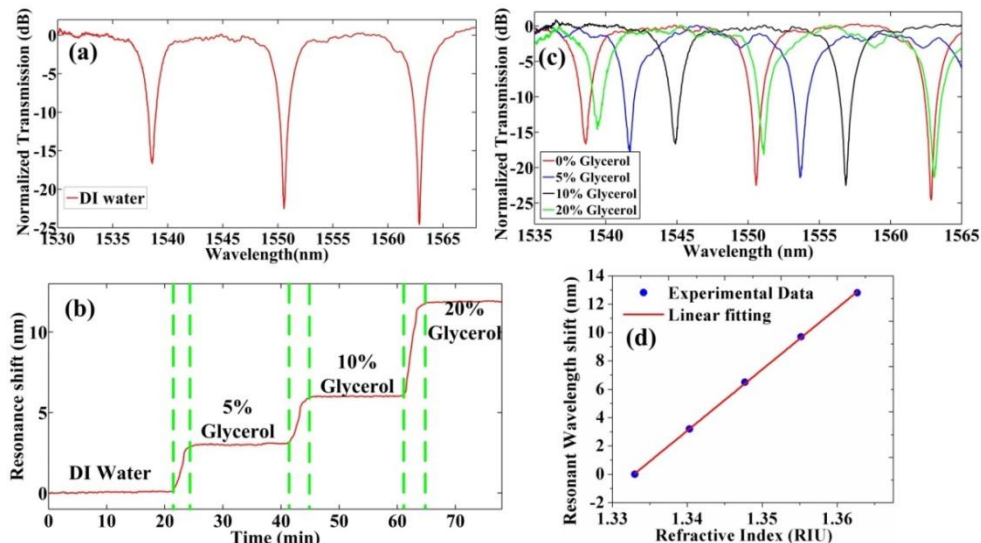


**Figure 8.** (a) Transmission spectrum of the fabricated TM mode SWG racetrack resonator in DI water. (b) Resonance shift for fabricated device with different concentration glycerol solutions.

(c) Shift of the transmission spectra for different concentration glycerol solutions (0%, 5%, 10% and 20%). (d) Fitting plot of resonance shifts.

The sensitivity of the device is characterized by monitoring resonance shift when different concentration solutions are consecutively injected onto the surface of the fabricated samples through microfluidic channels. The chip stage is kept at $25^o$C with a temperature controller. The results are shown in Fig. 8(b). The vertical dotted green line represents the time when new concentration of glycerol solution is injected. Fig. 8(c) shows the stabilized transmission spectra after the new concentration solutions are applied. The refractive indices for 0%, 5%, 10%, and 20% concentration solutions of glycerol are 1.333, 1.340, 1.347 and 1.362, respectively [32]. Fig. 8(d) is the plot of linear fitting of the resonance shift in relation to the change of refractive index of the solution. The bulk sensitivity of the fabricated devices is about 429.7nm/RIU. The sensitivity of the fabricated devices with a relative larger waveguide width (600 nm) and smaller radius of racetrack (10μm), is larger than 402nm/RIU in the SWG ring with the waveguide width of 500 nm and 30μm radius of ring. The intrinsic detection limit (iDL) of the proposed structure is $3.71 \times 10^{-4}$ RIU, lower than that in the ring resonator of $5.5 \times 10^{-4}$ RIU [24]. The sensitivity of the SWG racetrack resonator is larger than that of TM mode strip waveguide ring resonators with waveguide thicknesses of 150 nm (247nm/RIU) and 220nm (238nm/RIU) [24]. The bulk sensitivity can be further improved by decreasing the Si duty cycle and the width of waveguide to increase the mode volume overlap. Furthermore, compared to the ring resonator (radius of 12.1μm) with the same circumference (75.8μm), the radius of racetrack resonator (10μm) is reduced by 17.4%, and the footprint is reduced by 9.5%, which further improves the packing density of optical sensors in a lab-on-chip system.

## 4. CONCLUSIONS

In conclusion, SWG microring resonator biosensors possess unique property of thickness-independent surface sensitivity and enhanced sensitivity compared to conventional microring resonators. Due to periodic pillar structure in the propagation direction, the effective sensing region is greatly extended, including not only on top and side of the waveguide, but also the space on the propagation path between the periodic pillars. Biosensing experiments on both SWG microring and conventional microring demonstrated the superior surface sensing capability of the SWG waveguide. We experimentally demonstrated miRNA detection at 1nM concentration with TE-polarized SWG ring resonators. We also demonstrated a compact and highly sensitive TM-polarized SWG racetrack ring resonator that is more tolerant to design variations. The sensitivity can be further improved with more aggressive mode volume overlap and more strict control of fabrication.

## ACKNOWLEDGEMENTS

## REFERENCES

1. M. C. C. Estevez, M. Alvarez, and L. M. M. Lechuga, "Integrated optical devices for lab-on-a-chip biosensing applications," Laser Photon. Rev. **6**, 463 (2012).

2. V. Passaro, C. Tullio, B. Troia, M. Notte, G. Giannoccaro, and F. Leonardis, "Recent Advances in Integrated Photonic Sensors," Sensors **12**, 15558 (2012).

3. F. Vollmer, L. Yang, and S. Fainman, "Label-free detection with high-Q microcavities: A review of biosensing mechanisms for integrated devices," Nanophotonics **1**, 267 (2012).

4. B. Zhang, A. W. Morales, R. Peterson, L. Tang, and J. Y. Ye, "Label-free detection of cardiac troponin I with a photonic crystal biosensor," Biosens. Bioelectron. **58**, 107 (2014).

5. A. A. Yanik, M. Huang, A. Artar, T.-Y. Chang, and H. Altug, "Integrated nanoplasmonic-nanofluidic biosensors with targeted delivery of analytes," Appl. Phys. Lett. **96**, 21101 (2010).

6. M. Iqbal, M. A. Gleeson, B. Spaugh, F. Tybor, W. G. Gunn, M. Hochberg, T. Baehr-Jones, R. C. Bailey, and L. C. Gunn, "Label-Free Biosensor Arrays Based on Silicon Ring Resonators and High-Speed Optical Scanning Instrumentation," IEEE J. Sel. Top. Quantum Electron. **16**, 654 (2010).

7. C.-Y. Chao and L. J. Guo, "Biochemical sensors based on polymer microrings with sharp asymmetrical resonance," Appl. Phys. Lett. **83**, 1527 (2003).

8. M. S. McClellan, L. L. Domier, and R. C. Bailey, "Label-free virus detection using silicon photonic microring resonators," Biosens. Bioelectron. **31**, 388 (2012).

9. S. Janz, D.-X. Xu, M. Vachon, N. Sabourin, P. Cheben, H. McIntosh, H. Ding, S. Wang, J. H. Schmid, A. Delâge, J. Lapointe, A. Densmore, R. Ma, W. Sinclair, S. M. Logan, R. Mackenzie, Q. Y. Liu, D. Zhang, G. Lopinski, O. Mozenson, M. Gilmour, and H. Tabor, "Photonic wire biosensor microarray chip and instrumentation with application to serotyping of Escherichia coliisolates.," Opt. Express **21**, 4623 (2013).

10. X. Wei, J. W. Mares, Y. Gao, D. Li, and S. M. Weiss, "Biomolecule kinetics measurements in flow cell integrated porous silicon waveguides," Biomed. Opt. Express **3**, 1993 (2012).

11. W.-C. Lai, S. Chakravarty, Y. Zou, Y. Guo, and R. T. Chen, "Slow light enhanced sensitivity of resonance modes in photonic crystal biosensors," Appl. Phys. Lett. **102**, 41111 (2013).

12. F. Liang, N. Clarke, P. Patel, M. Loncar, and Q. Quan, "Scalable photonic crystal chips for high sensitivity protein detection.," Opt. Express **21**, 32306 (2013).

13. H. Yan, Y. Zou, S. Chakravarty, C.-J. Yang, Z. Wang, N. Tang, D. Fan, and R. T. Chen, "Silicon on-chip bandpass filters for the multiplexing of high sensitivity photonic crystal microcavity biosensors," Appl. Phys. Lett. **106**, 121103 (2015).

14. M. Sumetsky, "Optimization of optical ring resonator devices for sensing applications," Opt. Lett. **32**, 2577 (2007).

15. T. Claes, J. G. Molera, K. De Vos, E. Schacht, R. Baets, and P. Bienstman, "Label-Free Biosensing With a Slot-Waveguide-Based Ring Resonator in Silicon on Insulator," IEEE Photonics J. **1**, 197 (2009).

16. J.-W. Hoste, S. Werquin, T. Claes, and P. Bienstman, "Conformational analysis of proteins with a dual polarisation silicon microring.," Opt. Express **22**, 2807 (2014).

17. C. Qiu, J. Chen, and Q. Xu, "Ultraprecise measurement of resonance shift for sensing applications.," Opt. Lett. **37**, 5012 (2012).

18. S. T. Fard, V. Donzella, S. A. Schmidt, J. Flueckiger, S. M. Grist, P. Talebi Fard, Y. Wu, R. J. Bojko, E. Kwok, N. A. F. Jaeger, D. M. Ratner, and L. Chrostowski, "Performance of ultra-thin SOI-based resonators for sensing applications," Opt. Express **22**, 14166 (2014).

19. P. J. Bock, P. Cheben, J. H. Schmid, J. Lapointe, A. Delâge, S. Janz, G. C. Aers, D.-X. Xu, A. Densmore, and T. J. Hall, "Subwavelength grating periodic structures in silicon-on-insulator: a new type of microphotonic waveguide.," Opt. Express **18**, 20251 (2010).

20. J. Gonzalo Wangüemert-Pérez, P. Cheben, A. Ortega-Moñux, C. Alonso-Ramos, D. Pérez-Galacho, R. Halir, I. Molina-Fernández, D.-X. Xu, and J. H. Schmid, "Evanescent field waveguide sensing with subwavelength grating structures in silicon-on-insulator," Opt. Lett. **39**, 4442 (2014).

21. V. Donzella, A. Sherwali, J. Flueckiger, S. M. Grist, S. T. Fard, and L. Chrostowski, "Design and fabrication of SOI micro-ring resonators based on sub-wavelength grating waveguides," Opt. Express **23**, 4791 (2015).

22. J. D. A. S. A. Erenguel, A. L. O. R. Oñux, J. E. A. N. A. R. C. F. Édéli, P. A. C. Heben, Í. Ñ. M. O. Ernández, and R. O. H. Alir, "Controlling leakage losses in subwavelength grating silicon metamaterial waveguides," Opt. Lett. **41**, 3443 (2016).

23. J. Flueckiger, S. Schmidt, V. Donzella, A. Sherwali, D. M. Ratner, L. Chrostowski, and K. C. Cheung, "Sub-wavelength grating for enhanced ring resonator biosensor," Opt. Express **24**, 15672 (2016).

24. S. Schmidt, J. Flueckiger, W. Wu, S. M. Grist, S. Talebi Fard, V. Donzella, P. Khumwan, E. R. Thompson, Q. Wang, P. Kulik, X. Wang, A. Sherwali, J. Kirk, K. C. Cheung, L. Chrostowski, and D. Ratner, "Improving the performance of silicon photonic rings, disks, and Bragg gratings for use in label-free biosensing," SPIE Proc. **9166**, 91660M (2014).

25. Z. Wang, X. Xu, D. Fan, Y. Wang, and R. T. Chen, "High quality factor subwavelength grating waveguide micro-ring resonator based on trapezoidal silicon pillars," Opt. Lett. **41**, 3375 (2016).

26. Z. Wang, X. Xu, D. Fan, Y. Wang, H. Subbaraman, and R. T. Chen, "Geometrical tuning art for entirely subwavelength grating waveguide based integrated photonics circuits," Sci. Rep. **6**, 24106 (2016).

27. J. A. Howarter and J. P. Youngblood, "Optimization of Silica Silanization by 3-Aminopropyltriethoxysilane," Langmuir **22**, 11142 (2006).

28. A. Subramanian, S. J. Kennel, P. I. Oden, K. B. Jacobson, J. Woodward, and M. J. Doktycz, "Comparison of techniques for enzyme immobilization on silicon supports," Enzyme Microb. Technol. **24**, 26 (1999).

29. S. M. Grist, S. a Schmidt, J. Flueckiger, V. Donzella, W. Shi, S. Talebi Fard, J. T. Kirk, D. M. Ratner, K. C. Cheung, and L. Chrostowski, "Silicon photonic micro-disk resonators for label-free biosensing," Opt. Express **21**, 7994 (2013).

30. N. S. K. Gunda, M. Singh, L. Norman, K. Kaur, and S. K. Mitra, "Optimization and characterization of biomolecule immobilization on silicon substrates using (3-aminopropyl) triethoxysilane (APTES) and glutaraldehyde linker," Appl. Surf. Sci. **305**, 522 (2014).

31. J. Vörös, "The density and refractive index of adsorbing protein layers.," Biophys. J. **87**, 553 (2004).

32. L. F. Hoyt, "New Table of the Refractive Index of Pure Glycerol at 20°C," Ind. Eng. Chem. **26**, 329 (1934).

33. N. Mortensen, S. Xiao, and J. Pedersen, "Liquid-infiltrated photonic crystals: enhanced light-matter interactions for lab-on-a-chip applications," Microfluid. Nanofluid. **4**, 117 (2008).

34. L. C. Andreani, "Photonic bands and radiation losses in photonic crystal waveguides," phys. stat. sol.(b), **234**, 139 (2002).

35. M. H. Lukas Chrostowski, Silicon Photonics Design, (academic, 2013).

36. J. C. Slater, Microwave Electronics, (academic, 1950).

37. W. Bogaerts, P. D. Heyn, T. V. Vaerenbergh, K. D. Vos, S. K. Selvaraja, T. Claes, P. Dumon, P. Bienstman, D. V. Thourhout, R.Baets, "Silicon microring resonators," Laser Photonics Rev. **6**, 47 (2012).